

Effects of Epistemic Uncertainty on Empennage Loads During Dynamic Maneuvers

Ruxandra Duca,^{*} Darshan Sarojini,^{*} Sebastian Bloemer,[†] Imon Chakraborty,[‡]
Simon Briceno,[§] and Dimitri N. Mavris[¶]

*Aerospace Systems Design Laboratory, School of Aerospace Engineering
Georgia Institute of Technology, Atlanta, Georgia, 30332*

The Federal Aviation Regulations contain descriptions of a number of dynamic maneuvers that may lead to the development of critical loads for aircraft structural components. The structural members must be sized and designed to withstand such loads, and this must be demonstrated as part of the certification process. Given the high costs of aircraft certification and the programmatic risk associated with design modifications necessitated during later design stages, there is currently a trend towards certification by analysis. Towards this end, from the structural loads perspective, there is a need for a framework that can simulate maneuvers and evaluate the structural loads thus developed. However, in the earlier phases of design, significant epistemic uncertainty may exist with regard to the aircraft mass properties and aerodynamic characteristics, which in turn lead to uncertainty in the maneuver loads. This work demonstrates a methodology that employs sensitivity and Monte Carlo analyses to assess how maneuvering structural loads are affected by uncertainty factors. These analyses are applied to a dynamic simulation model created to simulate a representative business jet performing a checked pitch maneuver. The resultant variability of critical structural loads provides insight into the areas where epistemic uncertainty should be reduced.

I. Introduction

The critical or sizing loads for major aircraft components (e.g., wings, horizontal stabilizer, and vertical stabilizer) often occur during dynamic maneuvers, in which the motion of the aircraft contributes significantly to the developed aerodynamic and inertial loads. Catastrophic failures may occur as a consequence of large, unforeseen dynamic loads, as evidenced by the in-flight vertical stabilizer failure on American Airlines Flight 587 (an Airbus A300B4 aircraft), where it was subsequently determined that dynamic loads developed on it due to the first officer's rapid, aggressive, and oscillatory rudder inputs in response to a wake turbulence encounter exceeded its ultimate design load limits.¹

Airworthiness requirements related to structural loads and integrity can, therefore, drive the design and sizing of structural components. In the United States, certification and airworthiness standards for transport category aircraft, including those pertaining to structural loads, are described in Part 25 of Title 14 of the Code of Federal Regulations (14 CFR Part 25). The regulatory entity for this is the Federal Aviation Administration (FAA), and the regulations are commonly called the Federal Aviation Regulations (FARs).²

During the certification process, compliance with applicable FARs must be demonstrated through a combination of computational analyses and physical testing in order to establish safety, durability, and reliability.^{3,4} Flight test campaigns, though necessary, impose a considerable burden on the manufacturer in terms of both time and cost, and any re-design or mitigation actions necessitated in this phase can result in

^{*}Graduate Research Associate, ASDL, School of Aerospace Engineering, Georgia Tech, AIAA Student Member

[†]Graduate Student, RWTH Aachen University, Germany

[‡]Research Engineer II, ASDL, School of Aerospace Engineering, Georgia Tech, AIAA Member

[§]Senior Research Engineer, ASDL, School of Aerospace Engineering, Georgia Tech, AIAA Senior Member

[¶]S.P. Langley Distinguished Regents Professor and Director of ASDL, Georgia Tech, AIAA Fellow

programmatic delays. There is, therefore, a need for a capability to computationally simulate and assess the structural loads arising from complex, dynamic maneuvers, with fidelity that is appropriate for facilitating Certification by Analysis. Such a capability permits the simulation and evaluation of a large number of scenarios (which may be either too numerous or too risky to be attempted during actual flight testing), thus helping to de-risk the aircraft's certification program.

In prior work by the authors,⁵ a three degree-of-freedom (3-DoF) aircraft simulation capability was developed in order to assess dynamic loads developed on the horizontal stabilizer of a representative business jet performing a *Checked Pitch Maneuver* in accordance with the pilot actions and test envelope specified in FAR § 25.331(c)(2). The simulation used information regarding aircraft mass properties as well as aerodynamic and propulsion characteristics, combined with models of pilot control action and the elevator flight control system to calculate the critical horizontal tail root loads (bending moment, torsional moment, and shear forces) and elevator hinge moment.

In the early phases of design, however, the aerodynamic characteristics and mass properties of the aircraft are subject to epistemic uncertainty. This is further amplified if the configuration of the aircraft is significantly different to previous designs from the manufacturer, since historical data may be less applicable. The uncertainty will translate to variability in the predicted structural loads during the performance of maneuvers. Naturally, it is desirable for the designer/analyst to know (i) the extent to which the different critical loads are impacted by uncertainty and (ii) the relative influence of the identified sources of uncertainty on the observed variability of the maneuver loads. These form the over-arching goals of this work, which streamlines and enhances the simulation capability developed in prior work.⁵

First, the epistemic uncertainty is represented through probability distributions that characterize the variability of mass properties and aerodynamic characteristics. In certain cases, the distributions apply to the characteristics themselves, and in other cases to variation factors of K-factors that modify the characteristics (as described subsequently). Second, a screening analysis is performed to determine a subset of factors that have non-negligible impact on the tracked responses (critical empennage structural loads). Finally, a Monte Carlo simulation is employed to propagate the uncertainty from the input variables to the responses of interest. This numerical experimentation technique consists of performing multiple deterministic analyses for random input variables sampled from a distribution.⁶ Consequently, the critical root loads are now represented by distributions rather than single values.

The presented approach is developed and tested using data corresponding to an aircraft from a business jet manufacturer's product line. The results to be presented in this paper will therefore be suitably modified or redacted where necessary in order to protect proprietary data corresponding to this aircraft's aerodynamics, mass properties, geometry, elastic characteristics, and performance envelope.

The remainder of the paper is organized as follows: Section II summarizes the development of the framework completed thus far. Section III Section IV describes the screening studies and sensitivity analysis. Section V presents the uncertainty analysis. Finally, Section VI provides a summary of the work.

II. Overview of Integrated Simulation Framework

The simulation framework developed in this work is shown using the extended Design Structure Matrix (xDSM)⁷ in Fig. 1 and described in the following sections. It uses MATLAB R2017b/Simulink 9.0 and is back-compatible with MATLAB R2017a/Simulink 8.9.

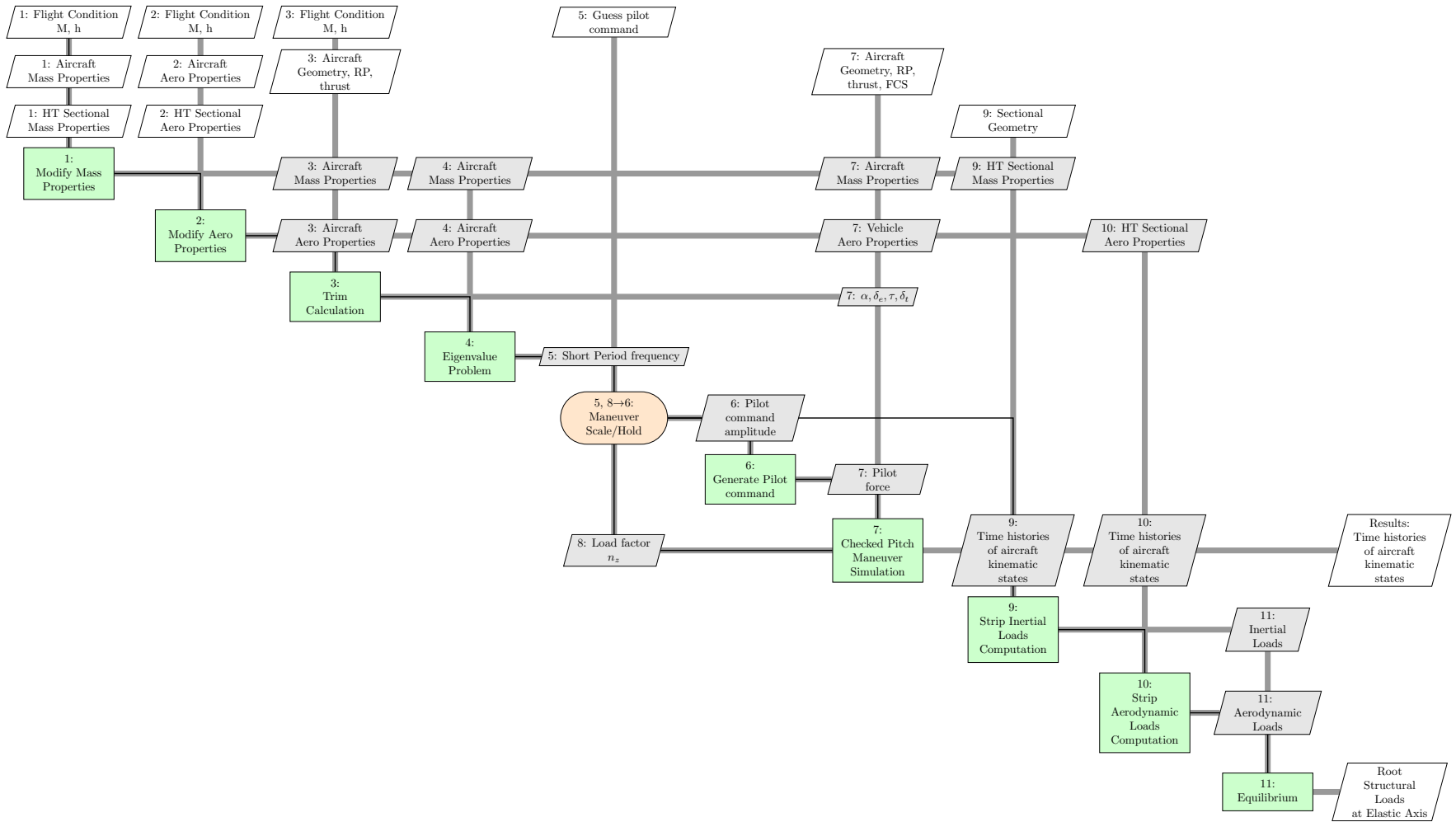


Figure 1: Checked pitch maneuver evaluation flowchart

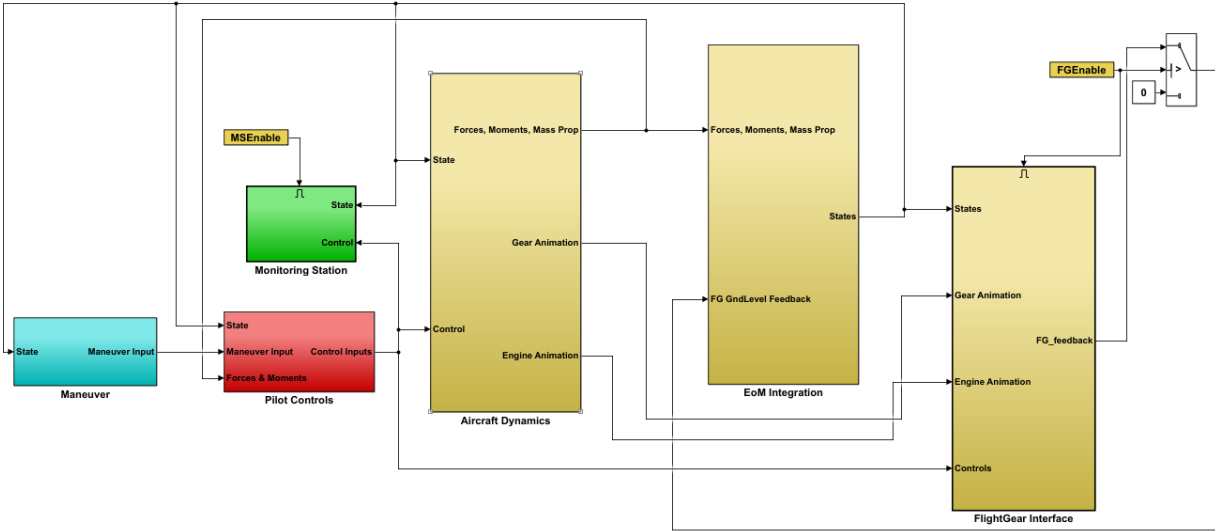


Figure 2: Top-level of Simulink model (Simulink 9.0 / MATLAB R2017b)

II.A. Inputs to the framework

The inputs required by the environment are shown in Fig. 1 as white trapezoids in the first 3 rows. They are listed below:

1. Flight condition: altitude and Mach number
2. Aircraft properties
 - (a) Mass properties: mass, center of gravity, moment of inertia
 - (b) Aircraft geometry and reference point
 - (c) Aerodynamic data
 - (d) Thrust data
 - (e) Flight control system (FCS) properties
3. Sectional properties
 - (a) Mass properties of each strip: mass, center of gravity, moment of inertia
 - (b) Strip geometry
 - (c) Strip aerodynamic data

If uncertainty analysis is to be performed, the inputs flow into the *Modify Aero Properties* and *Modify Mass Properties* blocks. These blocks vary the properties while ensuring consistency. They are explained in Section III.

II.B. Trim and Eigenvalue Problem

The mass and aerodynamic properties are then fed into the *Trim Calculation* block where the trim solution of the aircraft is found. This gives the angle of attack (α), elevator deflection (δ_e), throttle setting (τ), and trim tab deflection (δ_t). The mass and aerodynamic properties are also fed into the *Eigenvalue Problem* block which sets up the linear eigenvalue problem to find the undamped natural frequency of the aircraft's short period mode, which is required to generate control inputs for the checked pitch maneuver.

II.C. MATLAB/Simulink Flight Simulation Environment

Figure 2 shows the top-level of the Simulink flight simulation model. The *Maneuver* block contains Simulink elements that translate the language of the FARs of interest into corresponding actionable desired states or control inputs. The setup of this block, therefore, depends on the specific FAR being simulated. The *Pilot Controls* block contains the model of the human test pilot. Depending on the requirements of the specific FAR and the feedback of the current aircraft states, this block simulates the control actions of the pilot and generates corresponding control inputs.

The *Aircraft Dynamics* block is a complex block that contains the aerodynamic, propulsion, and structural loads modeling of the aircraft. The outputs from this block are the net external forces and moments on the aircraft as well as any mass properties updates. This information is used by the *EoM Integration* block to compute the time-evolution of the aircraft states by integrating the Equations of Motion (EoM). The Aircraft Dynamics block contains within it the *Aerodynamics & Propulsion* block and the *Structural Loads* block. The *Aerodynamics & Propulsion* block computes the forces and moments due to aerodynamics and propulsion. The summed forces and moments are added to the forces and moments due to gravity and then propagated to the *EoM Integration* block, where the 6-DoF rigid body equations of motion are used to obtain the time-evolution of the aircraft states $\vec{X}_{A/C}$ by integrating their time derivatives $\dot{\vec{X}}_{A/C}$. The distributed loads over the empennage strips is computed within the *Structural Loads* block, which enforces dynamic equilibrium conditions successively on empennage strips to obtain the root loads.

The *FlightGear Interface* block interfaces the Simulink model with FlightGear Flight Simulator (FGFS),⁸ generating a visual rendering of the aircraft's trajectory and motion within the FGFS environment. The customizable *Monitoring Station* block contains animated instruments (from Simulink *Aerospace Blockset*) and readouts of any aircraft parameters of interest. The *FlightGear Interface* and *Monitoring Station* blocks are used strictly to inspect the evolution of the simulation in real-time. They are deactivated (using the *FGEnable* and *MSEnable* flags respectively) when the simulation model is run in batch-mode.

The parameters required to initialize the Simulink model (e.g., vehicle aerodynamic characteristics and mass properties, trim solutions, etc.) are computed using MATLAB pre-processing scripts. Similarly, MATLAB post-processing scripts are used to process, query, and modify data generated from the simulation.

II.C.1. Pilot Model and Control Scaling Logic

The checked pitch maneuver is described in FAR §25.331(c)(2) in terms of the control deflection required as a function of time, the load factor, and the permissible pilot force. Starting from steady, level, flight between V_A (maneuver speed) and V_D (design dive speed), the maneuver is commenced with a target control application of a sinusoidal nature, given by

$$\delta(t) = \delta_{av} \sin(\omega t), \quad \text{for } 0 \leq t \leq \frac{3\pi}{2\omega} \quad \text{and} \quad \omega \leq \frac{\pi V}{2V_A}. \quad (1)$$

To simulate the actions of a human pilot trying to match the FAR-prescribed control input, a proportional-integral-derivative (PID) controller is used. The action of the controller is to modulate the force applied by the pilot in order to minimize a suitably defined error. The output force is bounded within the permissible ranges specified in FAR §25.397(c). The pilot model is capable of tracking either (a) a prescribed control motion or (b) responding to the evolution of aircraft state. The pilot model outputs a force F_{pilot} to minimize the error between the target and actual control application. The maximum available displacement of the flight deck pitch control δ_{av} may be limited by the flight control system ($\delta_{av} = |\delta_{max} - \delta_{e,trim}|$) or by pilot effort in accordance with FAR §25.397(b), both of which are taken into account. The circular frequency ω is taken equal to the undamped natural frequency of the short period rigid mode of the airplane.

The amplitude δ_{av} is iteratively scaled to the extent necessary to ensure that a threshold load factor is met but not exceeded (2.5 g for nose-up maneuvers and 0 g for nose-down maneuvers). If the airplane response to this control application does not achieve the prescribed limit load factors, then the control is held for the duration required to achieve the target load factor, but not in excess of five seconds. This iterative process is shown in Fig. 1 as *Maneuver Scale/Hold* loop.

II.C.2. Flight Control System Modeling

The pilot's elevator control inputs is related to the corresponding elevator deflection through a simplified model of the elevator control system dynamics. The normalized longitudinal control input $x_e \in [-1, 1]$

is assumed to be related to the control surface deflection $\delta_e \in [\delta_{e,min}, \delta_{e,max}]$ through a constant gearing ratio G . The control effort F_{pilot} applied by the pilot is assumed to be amplified by the action of hydraulic actuators by a gain factor k . The governing equations for the elevator flight control system are given by

$$m_t \ddot{x}_{cs} = F_{pilot} - F_C - c_\ell \dot{x}_e \quad (2)$$

$$I_e \ddot{\delta}_e = M_C + H_e - c_r \dot{\delta}_e \quad (3)$$

$$M_C G = (1 + k) F_C \quad (4)$$

$$G = \frac{\delta_e}{x_e} = \frac{\dot{\delta}_e}{\dot{x}_e} = \frac{\ddot{\delta}_e}{\ddot{x}_e} \quad (5)$$

Equation 2 is a force balance applied to the translating elements of the control system of effective mass m_t , with c_ℓ used to model friction losses. Equation 3 is a moment balance applied to the control surface hinge line, with I_e the elevator moment of inertia and H_e the aerodynamic hinge moment about its hinge line, and c_r is used to model rotational friction losses. Equation 4 relates the control system force F_C , moment M_C , and gearing ratio G . The latter relates cockpit control movements to control surface deflections as per Equation 5. Combining the above yields a second-order ordinary differential equation for the control surface motion:

$$\left[I_e + \frac{m_t(1+k)}{G^2} \right] \ddot{\delta}_e + \left[c_r + \frac{c_\ell(1+k)}{G^2} \right] \dot{\delta}_e = F_{pilot} \left[\frac{1+k}{G} \right] + H_e \quad (6)$$

The equations are implemented in the *Pilot Controls* block shown in Fig. 2

II.C.3. 6-DoF Equations of Motion (within EoM Integration Block)

The implementation of the equations of motion is similar to that within the *Custom Variable Mass 6DOF (Euler Angles)* of the *Aerospace Blockset*, but the equations are written with respect to a fixed reference point O rather than the center-of-gravity (CG). This enables, for instance, the dynamics of a moving CG (e.g., due to decreasing fuel mass or fuel transfer) to be modeled. The force and moment equations in vector form are given below.

$$\begin{aligned} \vec{F}_{tot} &= m \left(\dot{\vec{V}}_0 + \vec{\Omega} \times \vec{V}_0 + \ddot{\vec{r}}_{oc} + \dot{\vec{\Omega}} \times \vec{r}_{oc} + 2 \vec{\Omega} \times \dot{\vec{r}}_{oc} + \vec{\Omega} \times (\vec{\Omega} \times \vec{r}_{oc}) \right), \\ \vec{M}_{o,tot} &= \bar{I}_o \dot{\vec{\Omega}} + \vec{\Omega} \times \bar{I}_o \vec{\Omega} + m \vec{r}_{oc} \times \left(\dot{\vec{V}}_0 + \vec{\Omega} \times \vec{V}_0 \right), \end{aligned} \quad (7)$$

where m is the vehicle mass, \bar{I}_o the inertia tensor computed with respect to reference point O, $\vec{V}_0 = \{u, v, w\}^T$ is the velocity of the reference point O and $\vec{\Omega} = \{p, q, r\}^T$ is the angular velocity of the aircraft. The position of the CG with respect to the reference point O is given by \vec{r}_{oc} . The special case of a non-moving CG coinciding with the reference point O is obtained by setting $\vec{r}_{oc} = \dot{\vec{r}}_{oc} = \ddot{\vec{r}}_{oc} = 0$. All tensor quantities in Equation 7 are resolved in the aircraft body-fixed basis, with x-axis aligned with the longitudinal axis pointing forward, and y-axis towards the starboard wing.

Standard kinematic relationships are used to obtain the derivatives of the Euler angles ϕ , θ , and ψ from the angular rates p , q , and r , and also derivatives of the position x_0 , y_0 , and z_0 of the reference point O from the velocities u , v , and w . The resulting system of 12 nonlinear ordinary differential equations (in $u, v, w, p, q, r, \Phi, \Theta, \Psi, x_0, y_0, z_0$) for six degrees-of-freedom rigid body motion is numerically integrated to obtain the motion history of the aircraft during the maneuver.

II.C.4. Geometry and Mass Properties Definition

At the aircraft-level, the mass properties definition involves overall vehicle mass, CG location, and inertia tensor components specified for all load-outs/configurations of interest (as shown in Table 1). Given the duration of most maneuvers (order of seconds), no variation of aircraft mass due to fuel consumption is modeled, and a constant mass is assumed. The same argument applies to the aircraft inertia tensor, whose elements are computed with respect to the reference point and expressed in the body-fixed axis system.

$$\bar{I}_o = \begin{bmatrix} I_{xx} & I_{xy} & I_{zx} \\ I_{xy} & I_{yy} & I_{yz} \\ I_{zx} & I_{yz} & I_{zz} \end{bmatrix} \quad (8)$$

Table 1: Weight configurations

Config.	Mass (m)	CG Loc. (\vec{r}_{oc})			Inertia (\bar{I}_o)					
		x_{oc}	y_{oc}	z_{oc}	I_{xx}	I_{yy}	I_{zz}	I_{xy}	I_{yz}	I_{zx}
1
...
n

The lifting surfaces and the fuselage are each divided into multiple sections, and for each section, mass properties information similar to that shown in Table 1 is specified. As described subsequently, this breakdown of mass properties is used for the computation of inertial loads during maneuvers.

II.C.5. Aerodynamic Modeling

The aerodynamic force and pitching moments are written as build-ups using the aerodynamic coefficients of the aircraft and the angle of attack and elevator deflection. The normal force N_{aero} and pitching moment M_{aero} are built up as

$$N_{aero} = \bar{q}S \left(C_{N_0}(M_\infty) + C_{N_\alpha}(M_\infty) \alpha + C_{N_{\alpha_{tail}}}(M_\infty) \alpha_{tail} + C_{N_{\delta_e}}(M_\infty) \delta_e \right), \quad (9)$$

$$M_{aero} = \bar{q}S\bar{c} \left(C_{m_0}(M_\infty) + C_{m_\alpha}(M_\infty) \alpha + C_{m_{\alpha_{tail}}}(M_\infty) \alpha_{tail} + C_{m_{\delta_e}}(M_\infty) \delta_e \right), \quad (10)$$

where \bar{q} is the dynamic pressure, S the wing planform area, \bar{c} the wing mean aerodynamic chord, α the angle of attack of the aircraft, (M_∞) the freestream Mach number, and δ_e the elevator angle. The angle of attack of the tail, α_{tail} is computed as

$$\alpha_{tail} = \alpha + i_t - \varepsilon + \frac{q\ell_t}{V_\infty}, \quad (11)$$

where i_t is the stabilizer setting angle, V_∞ the freestream velocity, and q the pitch rate. The tail downwash ε is computed as $\varepsilon = \varepsilon_0(M_\infty) + \varepsilon_\alpha(M_\infty) \alpha$. Lookup tables for the following aerodynamic coefficients as a function of Mach number were made available by a business jet manufacturer: $C_{N_0}(M_\infty)$, $C_{N_\alpha}(M_\infty)$, $C_{N_{\alpha_{tail}}}(M_\infty)$, $C_{N_{\delta_e}}(M_\infty)$, $C_{m_0}(M_\infty)$, $C_{m_\alpha}(M_\infty)$, $C_{m_{\alpha_{tail}}}(M_\infty)$, $C_{m_{\delta_e}}(M_\infty)$, $\varepsilon_0(M_\infty)$, and $\varepsilon_\alpha(M_\infty)$. Additionally, the coefficients pertaining to the horizontal stabilizer were provided on a *per strip* basis as well, to be used for the calculation of distributed aerodynamic loads on the stabilizer. These lookup tables were used to generate gridded interpolants (MATLAB: *griddedInterpolant*) queried in terms of freestream Mach number. The most significant contributor to the aerodynamic axial force $F_{x,aero}$ is the aerodynamic drag experienced by the aircraft. However, no proprietary drag data was used in the aerodynamic modeling, due to its highly sensitive nature. Instead, a NASA legacy tool named FLOPS was used to estimate the aircraft drag characteristics (for details, see Goron et.al.⁵), yielding the axial aerodynamic force A_{aero} . The computed aerodynamic forces were transferred to the body-fixed axes as $F_{x,aero} = -A_{aero}$, $F_{z,aero} = -N_{aero}$, $M_{y,aero} = M_{aero}$.

II.C.6. Propulsion System Modeling

The thrust is found by interpolation between the minimum and maximum thrust values at the given flight conditions, based on the throttle setting τ , as seen in Equation 12. The minimum and maximum thrust values are functions of altitude and Mach number and are queried from look-up tables.

$$T(\tau, h, M) = T_{min}(h, M) + \tau[T_{max}(h, M) - T_{min}(h, M)] \quad (12)$$

The moment due to thrust is also considered by assuming the thrust force parallel to the body-fixed x-axis and computing the position of the thrust application point relative to the aircraft fixed reference point.

II.C.7. Structural loads analysis

To obtain the distributed aerodynamic, gravity, and inertial loads on the horizontal stabilizer, and in turn the root loads (shear, bending, and torsion), as well as the elevator hinge moment, the strip method is used. The horizontal stabilizer is divided into sections, or strips, with known aerodynamic and mass properties.

Then, dynamic equilibrium criteria are imposed on each strip, starting from the tip where the boundary conditions are known, and moving towards the root. Fig. 3 depicts a strip ‘ k ’ with the aerodynamic force $\vec{F}_{a,0}^{(k)}$ (with faired elevator), the incremental change in aerodynamic force due to elevator deflection $\Delta\vec{F}_{a\delta e}^{(k)}$, the net aerodynamic pitching moment $\vec{M}_a^{(k)}$, gravitational force $\vec{F}_g^{(k)}$ (at strip CG), inertial force $\vec{F}_i^{(k)}$ (at strip CG), and moment $\vec{M}_i^{(k)}$, as well as the reaction forces $\vec{F}_r^{(k)}$, $\vec{F}_r^{(k+1)}$ and moments $\vec{M}_r^{(k)}$, $\vec{M}_r^{(k+1)}$ at the two ends.

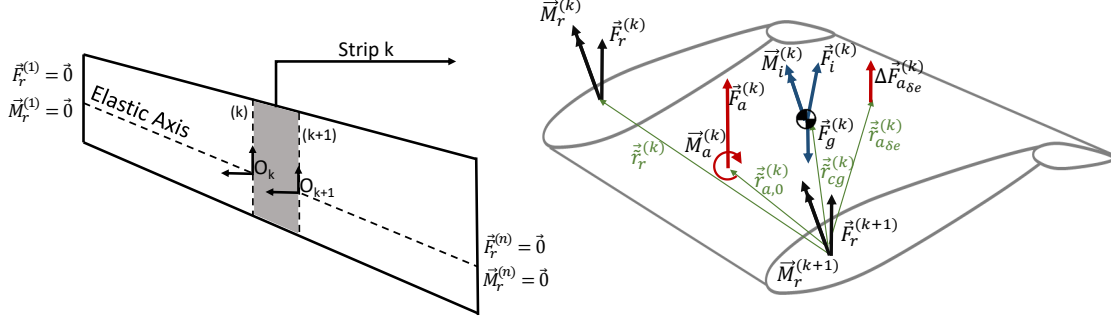


Figure 3: Strip method - applying dynamic equilibrium on each strip to obtain reaction loads⁵

To apply strip-wise equilibrium, all forces and moments on each strip are first computed. Each horizontal tail section experiences a normal force and a pitching moment due to the angle of attack of the tail, as well as an incremental force contribution due to the elevator deflection. These aerodynamic quantities are found using sectional aerodynamic coefficients in conjunction with the time histories of the aircraft states, as described in the equations below:

$$N_{strip}^{(k)} = \bar{q} * C_{N,strip}^{(k)} * S_{strip}^{(k)} \quad (13)$$

$$M_{strip}^{(k)} = \bar{q} * C_{m,strip}^{(k)} * S_{strip}^{(k)} * \bar{c}_{strip}^{(k)} \quad (14)$$

$$\Delta N_{strip}^{(k)} = \bar{q} * \Delta C_{N,strip,\delta e}^{(k)} * S_{strip}^{(k)} \quad (15)$$

The gravitational force is simply the weight of each strip, resolved along the axes of interest. To be able to use the concept of *dynamic equilibrium*, the accelerations are converted to inertial forces and moments using D’Alembert’s principle. Once these loads are known on each strip, the following force and moment balances are used to calculate the reaction force $\vec{F}_r^{(k+1)}$ and moment $\vec{M}_r^{(k+1)}$ at the new boundary. The moment balance includes additional terms due to the placement of the forces.

$$\vec{F}_r^{(k+1)} - \vec{F}_r^{(k)} + \vec{F}_{a,0}^{(k)} + \Delta\vec{F}_{a\delta e}^{(k)} + \vec{F}_i^{(k)} + \vec{F}_g^{(k)} = \vec{0} \quad (16)$$

$$\vec{M}_r^{(k+1)} - [\vec{M}_r^{(k)} + \vec{r}_r^{(k)} \times \vec{F}_r^{(k)}] + [\vec{M}_{a,0}^{(k)} + \vec{r}_{a,0}^{(k)} \times \vec{F}_{a,0}^{(k)}] + [\vec{r}_{a\delta e}^{(k)} \times \Delta\vec{F}_{a\delta e}^{(k)}] + [\vec{M}_i^{(k)} + \vec{r}_i^{(k)} \times \vec{F}_i^{(k)}] + [\vec{r}_{cg}^{(k)} \times \vec{F}_g^{(k)}] = \vec{0} \quad (17)$$

These relationships are applied at each strip successively from outboard to inboard until root reactions are obtained. The computations are performed at every time step throughout the maneuver. Thus, time histories of both the root loads and the loads on each strip are obtained. After performing these computations for all flight conditions, the most severe empennage loads and the corresponding flight conditions and pilot inputs are identified.

III. Uncertainty Analysis for Dynamic Loads

Since disciplinary knowledge and the fidelity of modeling/analysis tools may be limited in the early phases of design, the resulting epistemic uncertainty limits the usefulness of deterministic analyses as a basis for decision-making. A probabilistic representation of the input parameters can lead to a better understanding of the responses and their variability.⁹ In this case, a distribution of critical empennage loads may be obtained,

rather than a single-point values. The dynamics of the checked pitch maneuver do not include any changes in throttle setting or substantial velocity excursions that would change the thrust produced for a constant throttle setting. Therefore, the uncertainty analysis in this work focuses on variability of the mass properties and aerodynamic characteristics of the aircraft. The following sections expand on the different steps that will constitute the proposed uncertainty analysis: (i) method of varying mass properties (ii) method of varying aerodynamic properties, (iii) analysis flow for uncertainty analysis, and (iv) parallel execution setup.

III.A. Mass Properties Variation

The process for estimating and propagating the impact of changing aircraft mass properties begins by considering the baseline aircraft mass m_0^A as the sum of the tail-off mass m_0^{A-T} (A-T denotes *aircraft minus tail*) and the horizontal tail-only mass m_0^{ht} , i.e.,

$$m_0^A = m_0^{A-T} + m_0^{ht}, \quad (18)$$

where $(\)_0$ denotes a property where the value of the property is the baseline one. For example, m_0^{ht} is the baseline mass of the horizontal tail. If now, the mass of A-T changes to m^{A-T} ($\neq m_0^{A-T}$) while the tail-only mass changes to m^{ht} ($\neq m_0^{ht}$), then the calculation of the resulting total aircraft mass is straightforward:

$$m^A = m^{A-T} + m^{ht} \quad (19)$$

Calculation of the location of the CG is somewhat more involved, since it depends on not only the magnitude of mass but also its distribution. As such, it is possible (to an extent, at least) to vary net mass without changing CG location, or change CG location without varying net mass. This variation can be the result of relocating components in the aircraft, making changes to the tail design, or simply not having accurate information about the CG before the airframe and all components of the aircraft are manufactured. The variation of the CG can be captured in a manner similar to that of mass by considering the A-T and HT separately and varying their masses and CG. The baseline CG is given by

$$\vec{r}_0^A = \frac{m_0^{A-T} \vec{r}_0^{A-T} + m_0^{ht} \vec{r}_0^{ht}}{m_0^{A-T} + m_0^{ht}}. \quad (20)$$

By varying both masses and CG locations independently of each other, the formula for the modified CG of the entire aircraft becomes

$$\vec{r}^A = \frac{m^{A-T} \vec{r}^{A-T} + m^{ht} \vec{r}^{ht}}{m^{A-T} + m^{ht}}. \quad (21)$$

In the above, only some components of $\vec{r}^{A-T} = \{x^{A-T}, y^{A-T}, z^{A-T}\}$ and $\vec{r}^{ht} = \{x^{ht}, y^{ht}, z^{ht}\}^T$ were varied. At the A-T level, the longitudinal and vertical dimensions (x^{A-T} and z^{A-T} respectively) were varied with the assumption that the CG will stay at or close to centerline ($y^{A-T} \approx 0$) for a fairly symmetrical aircraft. For the horizontal stabilizer, variation of the vertical coordinate of the CG (z^{ht}) was assumed to be negligible, given the limited thickness of the airfoil, and was thus not varied. The longitudinal coordinate (x^{ht}) and lateral coordinate (y^{ht}) for each half of the tail were varied.

Finally, uncertainty in the moment of inertia of the entire airplane was modeled by independently varying A-T and HT moments of inertia, as well as taking into account the modifications in their masses and CG locations. The moment of inertia of the baseline aircraft computed with respect to the reference point $\vec{r}^{RP} = \{x^{RP}, y^{RP}, z^{RP}\}^T$ can be represented as

$$\begin{aligned} I_{yy_0}^{A/RP} &= I_{yy_0}^{A-T/RP} + I_{yy_0}^{ht/RP} \\ &= I_{yy_0}^{A-T/RP} + I_{yy_0}^{ht/CG} + m_0^{ht} \left[\left(x_0^{ht/CG} - x^{RP} \right)^2 + \left(z_0^{ht/CG} - z^{RP} \right)^2 \right]. \end{aligned} \quad (22)$$

Here, the notation $I_{yy_0}^{A/RP}$ denotes the baseline mass moment of inertia of the aircraft (A) about the y-axis passing through the reference point (RP). Similarly, $I_{yy_0}^{A-T/RP}$ is for the aircraft without the tail and $I_{yy_0}^{ht/RP}$ for the tail alone. The parallel axis theorem is employed to relate the moment of inertia of the HT about its own centroidal axes to its moment of inertia about axes located at the aircraft RP. When the masses,

CG locations, and centroidal moments of inertia of the A-T and HT deviate from the baseline values, the moment of inertia of the net aircraft is computed as

$$\begin{aligned} I_{yy}^{A/RP} &= I_{yy}^{A-T/RP} + I_{yy}^{ht/RP} \\ &= I_{yy}^{A-T/RP} + I_{yy}^{ht/CG} + m^{ht} \left[\left(x^{ht/CG} - x^{RP} \right)^2 + \left(z_0^{ht/CG} - z_0^{RP} \right)^2 \right], \end{aligned} \quad (23)$$

in which the z-coordinate of the horizontal stabilizer CG is left at its baseline value. Fig. 4 depicts the geometric dimensions involved in the evaluation of Eq. 23. Fig. 5 summarizes the eight mass property related quantities that were varied independently for uncertainty analyses.

The mass properties updates described above, which are at the aircraft level, need to be reflected into equivalent and consistent updates at the horizontal stabilizer strip level. Since such updates are not unique, a linear model for a change in mass $\Delta m^{ht(k)}$ as a function of the the CG location of strip i in the y-direction was developed:

$$\Delta m^{ht(k)} = a + b y_0^{ht(k)} \quad (24)$$

To identify the a and b parameters, two constraint conditions must be enforced. First, imposing overall mass preservation of half of the tail (containing n strips) yields

$$\begin{aligned} \frac{1}{2} m^{ht} &= \sum_i^n m^{ht(k)} \\ &= \sum_i^n \left[m_0^{ht(k)} + \Delta m^{ht(k)} \right] \\ &= \frac{1}{2} m_0^{ht} + na + b \sum_i^n y_0^{ht(k)}. \end{aligned} \quad (25)$$

Second, enforcing the overall lateral CG coordinate of half of the HT yields

$$\begin{aligned} y^{ht} &= \frac{\sum_i^n m^{ht(k)} y_0^{ht(k)}}{\sum_i^n m^{ht(k)}} \\ &= \frac{\sum_i^n \left[m_0^{ht(k)} + a + b y_0^{ht(k)} \right] y_0^{ht(k)}}{\sum_i^n \left[m_0^{ht(k)} + a + b y_0^{ht(k)} \right]} \\ &= \frac{\sum_i^n m_0^{ht(k)} y_0^{ht(k)} + a \sum_i^n y_0^{ht(k)} + b \sum_i^n \left(y_0^{ht(k)} \right)^2}{\frac{1}{2} m_0^{ht} + na + b \sum_i^n y_0^{ht(k)}} \end{aligned} \quad (26)$$

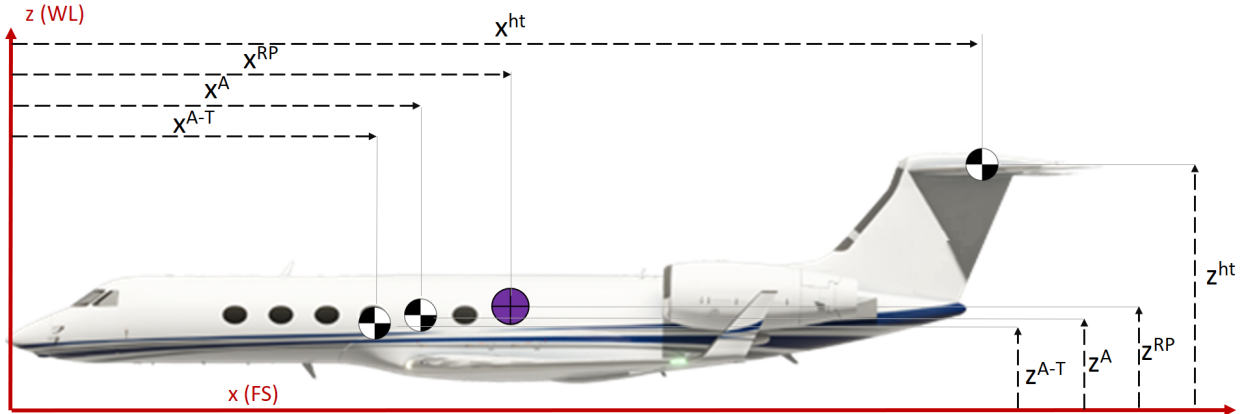


Figure 4: Coordinate system and geometric dimensions for mass properties updates

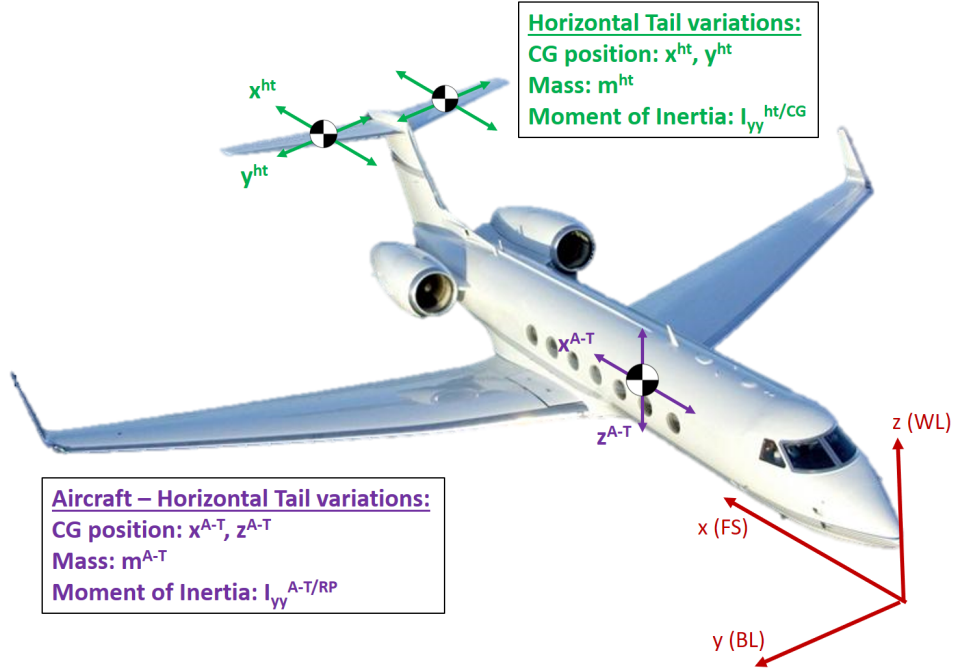


Figure 5: Summary of mass properties parameters that were varied for uncertainty analyses

Equations 25-26 together yield the matrix equation

$$\begin{bmatrix} n & \sum_i^n y_0^{ht(k)} \\ \sum_i^n y_0^{ht(k)} - ny^{ht} & \sum_i^n (y_0^{ht(k)})^2 - y^{ht} \sum_i^n y_0^{ht(k)} \end{bmatrix} \begin{bmatrix} a \\ b \end{bmatrix} = \begin{bmatrix} \frac{1}{2}(m^{ht} - m_0^{ht}) \\ \frac{1}{2}y^{ht}m_0^{ht} - \sum_i^n m_0^{ht(k)}y_0^{ht(k)} \end{bmatrix}, \quad (27)$$

which is solved to find a and b . Thereafter, each strip's mass is found as

$$m^{ht(k)} = m_0^{ht(k)} + a + b y_0^{ht(k)} \quad (28)$$

To obtain the overall change in the horizontal tail CG variation in the x-direction, the CG of each strip in this direction $x^{ht(k)}$ was modified in a mass preserving manner with a simple scaling

$$x^{ht(k)} = x_0^{ht(k)} \frac{x^{ht}}{x_0^{ht}}. \quad (29)$$

It can be verified that the CG of the entire horizontal tail is then recovered as

$$\frac{\sum_i^n m^{ht(k)} x^{ht(k)}}{\sum_i^n m^{ht(k)}} = \frac{\sum_i^n m^{ht(k)} x_0^{ht(k)} \frac{x^{ht}}{x_0^{ht}}}{\sum_i^n m_i} = \frac{x^{ht}}{x_0^{ht}} \cdot \frac{\sum_i^n m^{ht(k)} x_0^{ht(k)}}{\sum_i^n m^{ht(k)}} = \frac{x^{ht}}{x_0^{ht}} \cdot x_0^{ht} = x^{ht}. \quad (30)$$

To preserve the total tail moment of inertia $I_{yy}^{ht/CG}$ about its CG, this quantity was first expressed in terms of the moments of inertia of each strip about the strip CG using the parallel-axis theorem as

$$I_{yy}^{ht/CG} = \sum_i^n I_{yy}^{ht(k)/CG(k)} + \sum_i^n m^{ht(k)} [(x^{ht(k)} - x^{ht})^2 + (z^{ht(k)} - z^{ht})^2] \quad (31)$$

In this equation, the mass of each strip ($m^{ht(k)}$) has already been modified and is now set. So are the x-coordinates of each strip's CG ($x^{ht(k)}$) and the tail CG (x^{ht}). The z-coordinates are set to their default values since there is no variation allowed there. Thus, the only parameters to be varied at this point are the

moments of inertia of the strips about their own CG ($I_{yy}^{ht(k)/CG(k)}$). This is achieved through the simple scaling relationship

$$I_{yy}^{ht(k)/CG(k)} = k \cdot I_{yy_0}^{ht(k)/CG(k)} \quad (32)$$

The scaling factor k is found from Equations 31 and 32 as

$$k = \frac{I_{yy}^{ht/CG} - \sum_i^n m^{ht(k)} [(x^{ht(k)} - x^{ht})^2 + (z^{ht(k)} - z^{ht})^2]}{\sum_i^n I_{yy_0}^{ht(k)/CG}}. \quad (33)$$

III.B. Aerodynamic Characteristics Variation

The impact of uncertainty in aerodynamic characteristics was propagated through the use of K-factors. These factors are used to modify aerodynamic coefficients through a simple multiplication. Because the coefficients are queried from look-up tables based on the Mach number, using K-factors essentially scaled the dependent variables in the look-up tables (i.e., the variable being looked up). The K-factors were varied in this work are enumerated in Table 2. Once the change is applied, the coefficients are used in computing the aerodynamic forces and moments as described in Sec. II.C.5. As indicated in Table 2, the sectional data at the horizontal tail is also scaled to ensure a net effect that is consistent with the variation of the gross horizontal tail aerodynamic coefficients.

Table 2: K-factors used to propagate uncertainty in aerodynamic coefficients

Aerodynamic K-factor	Aero. Coeff. Modified	Sectional Coeff. Modified
$k_{C_{N0}}$	C_{N0}	
$k_{C_{N\alpha}}$	$C_{N\alpha}$	
$k_{C_{N\alpha T}}$	$C_{N\alpha T}$	$C_{N,strip}^{(k)}$
$k_{C_{N\delta e}}$	$C_{N\delta e}$	$\Delta C_{N,strip,\delta e}^{(k)}$
$k_{C_{M0}}$	C_{M0}	
$k_{C_{M\alpha}}$	$C_{M\alpha}$	
$k_{C_{M\alpha T}}$	$C_{M\alpha T}$	$C_{M,strip}^{(k)}$
$k_{C_{M\delta e}}$	$C_{M\delta e}$	
$k_{C_{he,\alpha T}}$	$C_{he,\alpha T}$	
$k_{C_{he,\delta e}}$	$C_{he,\delta e}$	

III.C. Analysis Flow for Uncertainty Analysis

When uncertainty analysis is to be performed, the *Modify Mass Prop* and *Modify Aero Prop* blocks shown in Fig. 1 are activated. These blocks take in the baseline aircraft and modify the gross and sectional aerodynamic characteristics as well as mass properties as per the relationships given in Sections III.A and III.B. With the modified aircraft mass and aerodynamic properties, a trim calculation is then performed. This yields the angle of attack, throttle setting, and elevator deflection required to trim at steady, level, unaccelerated flight at the given flight condition, as well as the elevator tab setting required to zero out the required control column (yoke) force. The eigenvalue problem is then solved for the longitudinal equations of motion to obtain the undamped natural frequency of the short period mode (ω in Eq. 1) corresponding to the current flight condition and aircraft mass and aerodynamic characteristics. The simulation of the checked pitch maneuver then occurs iteratively with the necessary scaling/holding of the control inputs until the target limit load factor conditions are met. The modified sectional mass and aero properties are used in *Strip Inertial Loads Computation* and *Strip Aerodynamic Loads Computation* blocks respectively.

III.D. Parallel Execution Setup

Performing uncertainty analysis entails running the simulation environment thousands of times. To speed up computation, the setup was parallelized using MATLAB's *spmd* (single program, multiple data) function.

This allows the user to specify the number of parallel workers and specify the allocation of cases to these workers. After parallelizing the framework, cases were run on desktop computers with specifications shown in Table 3 using four workers. On average, one run of the entire simulation (one pass through Figure 1) takes 9.3 seconds, yielding between 24-30 case evaluations per minute.

Table 3: Computer specifications for parallel setup

Processor	Intel(R) Core (TM) i7-2600 CPU @ 3.40 GHz (8 CPUs)
RAM	16 GB
Operating system	Windows 10 Enterprise 64-bit

IV. Screening Studies and Sensitivity Analysis

To identify which parameters contribute the most to the critical empennage loads, several representative cases were chosen from the deterministic analysis and screening studies were performed. The purpose of the screening test is to (i) determine whether all the epistemic uncertainty factors considered for mass properties and aerodynamics contribute significantly to the variability of the responses (empennage maneuver loads and (ii) identify the uncertainty factors that have the most significant impact on said variability. By systematically changing the variables using a 2-level full factorial Design of Experiments (DOE), their effect on the critical load values can be ascertained. A multi-variate linear regression is then used to understand how the responses vary with a variation in the inputs. This study revealed which variables have the greatest influence on critical loads and which variables could be set to default (constant) values and omitted from subsequent uncertainty analyses.

IV.A. Test Points and Weight Configurations for Screening Tests

Since, in general, the sensitivities may vary with flight condition, the screening test was performed for a number of points within the testing envelope (Fig. 6). The points were selected to include combinations of low and high altitudes and low and high Mach numbers and they spanned three different weight conditions: (i) mission configuration, (ii) heavy-weight forward CG, and (iii) lightweight aft CG. Additionally, points where critical loads occurred for each weight condition when no uncertainty was considered were also included, resulting in a total of 25 points. A screening test was performed for each of these points.

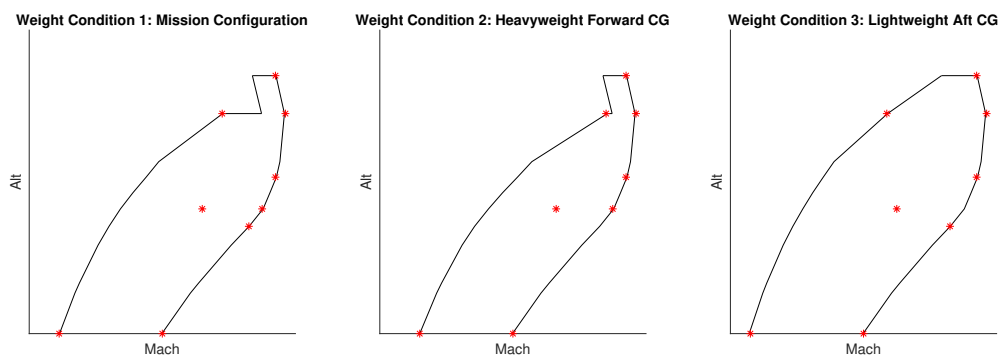


Figure 6: Test points for screening studies spanning various weight and flight conditions

The screening test began by establishing the ranges of uncertainty for each variable, with input from subject matter experts. To keep the dimensionality within reasonable bounds, the mass property and aerodynamic parameters were investigated separately at this stage. For each point in Fig. 6, a 2-level full factorial DOE was used to analyze all possible combinations of minima and maxima of the variables. The statistical analysis software JMP was used to create the DOE tables and to construct the regression. Since eight mass properties parameters were varied, there were $2^8 = 256$ cases plus one default case per test point. Similarly, there were $2^{10} = 1024$ cases plus the default one per point for screening of aerodynamic characteristics. Since the ranges of some quantities depend on the weight condition (m^{A-T} , x^{A-T} , z^{A-T} ,

and $I_{yy}^{A-T/RP}$), three DOEs were required for the mass properties screening studies. For each test point, depending on the corresponding weight condition, the appropriate DOE was appended. The ranges to be used in the DOE were obtained by taking the interval $[-3\sigma, +3\sigma]$, which includes over 99.7% of the population. In the following sections, all loads are expressed with the sign convention shown in Fig. 7.

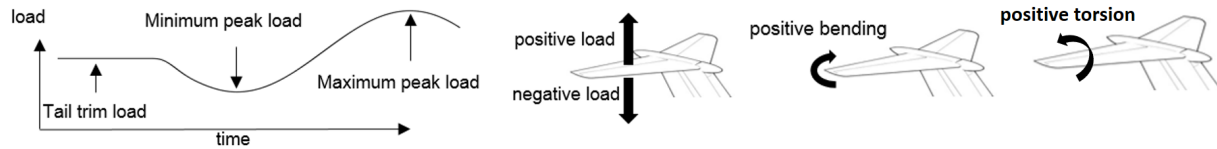


Figure 7: Sign convention for forces and moments

IV.B. Mass Properties Screening Results

The variable ranges that were employed for the mass properties screening test are summarized in Table 4. A multivariate linear regression was used to show how each parameter affects the variability of the critical loads within the ranges given.

Table 4: Ranges of parameters varied during mass properties screening test

	m^{ht}	x^{ht}	y^{ht}	$I_{yy}^{ht/CG}$	m^{A-T}	x^{A-T}	z^{A-T}	$I_{yy}^{A-T/RP}$
WC1	$\pm 30.1\%$	$\pm 0.57\%$	$\pm 14.9\%$	$\pm 0.29\%$	$\pm 8.11\%$	$\pm 1.75\%$	$\pm 4.248\%$	$\pm 0.707\%$
WC2	$\pm 30.1\%$	$\pm 0.57\%$	$\pm 14.9\%$	$\pm 0.29\%$	$\pm 6.69\%$	$\pm 1.72\%$	$\pm 3.75\%$	$\pm 0.55\%$
WC3	$\pm 30.1\%$	$\pm 0.57\%$	$\pm 14.9\%$	$\pm 0.29\%$	$\pm 10.49\%$	$\pm 1.76\%$	$\pm 4.33\%$	$\pm 0.75\%$

Figure 8 shows the results for mass properties screening using a profiler plot. In this type of plot, a

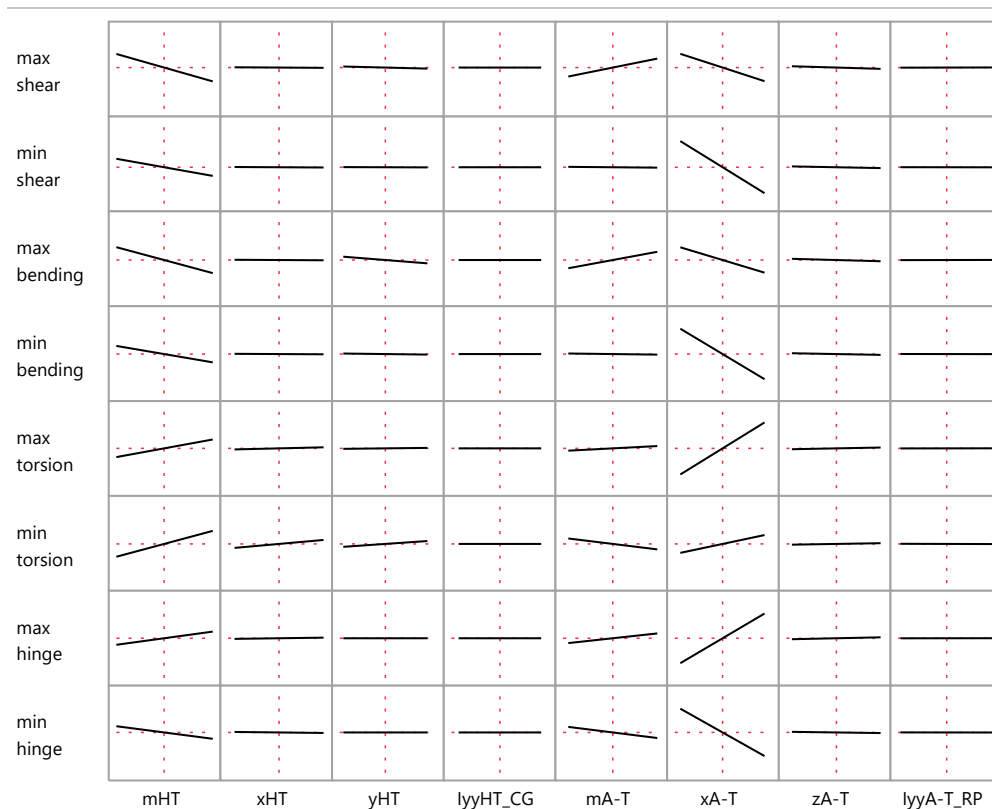


Figure 8: Profiler plot showing sensitivity of critical loads to mass property parameters

larger slope implies that the variable has greater impact on the response within the given range of variation. The variables that significantly affect the loads are the horizontal tail mass (m^{ht}), the A-T mass (m^{A-T}), and the x-coordinate of A-T (x^{A-T}), followed by smaller effects from tail CG coordinates in the x and y directions (x^{ht} , y^{ht}). An increasing (or decreasing) slope means that an increase in the variable leads to an increase (or decrease) in the response. In the following discussion, *increase* and *reduction* imply respectively upward and downward shifts in the load profile illustrated as part of the sign convention definition (Fig. 7).

It is seen that an increase in the horizontal tail mass (m^{ht}) leads to a reduction (negative slopes) in the peak root shear loads and bending moments. This is due to the fact that the increased mass of the tail results in larger gravitational forces that act downward, and also increased inertial forces during maneuvering which act out of phase with the aerodynamic loads. The increase in horizontal tail mass leads to an increase in the peak torsional loads (positive slope). This is due to the fact that the CG of each strip lies aft of the point about which torsional loads are computed. Therefore, an increase in downward-acting forces (e.g., gravitational) will result in positive torsional loads. The fact that the trendlines for the hinge moment are opposite of each other suggests that an increase in tail mass results in a larger magnitude of both maximum and minimum peaks (larger positive value, lower negative value). These trends can be explained based on the observed elevator application. For the increased mass case, larger elevator inputs are required to get the airplane to maneuver, leading to higher amplitude hinge moments (shown subsequently).

An important observation is that the x-coordinate of the A-T CG (x^{A-T}) has the most impact even though it is varied by less than 2% whereas the horizontal tail mass, which the next important contributor, is varied by a significant 30%. These trends were verified on profilers for all 25 points, for consistency, and they were all similar, suggesting that the sensitivity of the loads is independent of weight and flight condition. These observations are down to the relative extents to which these two parameters affect the dynamics of the maneuver.

The moment of inertia of the tail ($I_{yy}^{ht/CG}$) and A-T ($I_{yy}^{A-T/RP}$) do not seem to affect the loads responses at all. For a longitudinal maneuver in which the main motion is rotation about the y-axis, these two quantities are expected to have an important effect. However, the propagated uncertainty associated with them is rather small (less than 1% in each direction). The effect of these variations is negligible compared to the effect of other mass properties which vary by 5-30%. As a side note, appreciable variations in loads were obtained if the moments of inertia were varied more substantially.

To better compare the time-evolution of the maneuver when these parameters are varied, the time histories are plotted in Fig. 9 for variation of tail mass m^{ht} with other factors held constant. These curves bear out the observations made above based on Fig. 8. Additionally, it is seen that larger elevator inputs are necessitated by increased tail mass, thus resulting in increased magnitudes for the elevator hinge moment.

An extra check of the results can be made by looking at scatter plots of all the cases. (Fig. 10). While the results are not obvious in this type of plot, it does illustrate some trends which can be used to validate the interpretation of the profiler. The value from the deterministic analysis is shown as a black dot in the center which corresponds to all variables being set to their default values. The cases marked in red and yellow show the most drastic shift up and shift down respectively in peak bending moment. The cases marked blue and green show smaller changes from the default value. The scatter plots show that for a parameter with little influence, such as the moment of inertia of A-T ($I_{yy}^{A-T/RP}$), the drastic changes (red and yellow) occur at both ends of the moment of inertia range, minimum and maximum, suggesting that the effect is likely due to other factors. On the other hand, parameters with more influence, like the mass of the horizontal tail (m^{ht}) show a clear trend: increasing it (right side of the scatter plot) corresponds to drastic shift down of the bending moment (yellow) and decreasing it corresponds to drastic shift up (red). This is consistent with the profiler and was verified for all loads of interest.

Based on these results, only the mass and CG of the horizontal tail (both x and y) as well as the mass and x-coord of the CG of A-T were retained for uncertainty analysis (m^{ht} , x^{ht} , y^{ht} , m^{A-T} , x^{A-T}). The remaining parameters were set to their original (default) values, as it was found that they did not significantly affect the variabilities of the responses.

IV.C. Aerodynamic Characteristics Screening Results

A similar process to that for mass properties was followed to understand how aerodynamic characteristics affect critical loads. The aerodynamic coefficient variation is shown in Table 5, where a variation of a coefficient by, for instance, +5% translates into a K-factor of 1.05 scaling the coefficient look-up table, and so on. Figure 11 shows the profiler plot for loads sensitivity to aerodynamic K-factors.

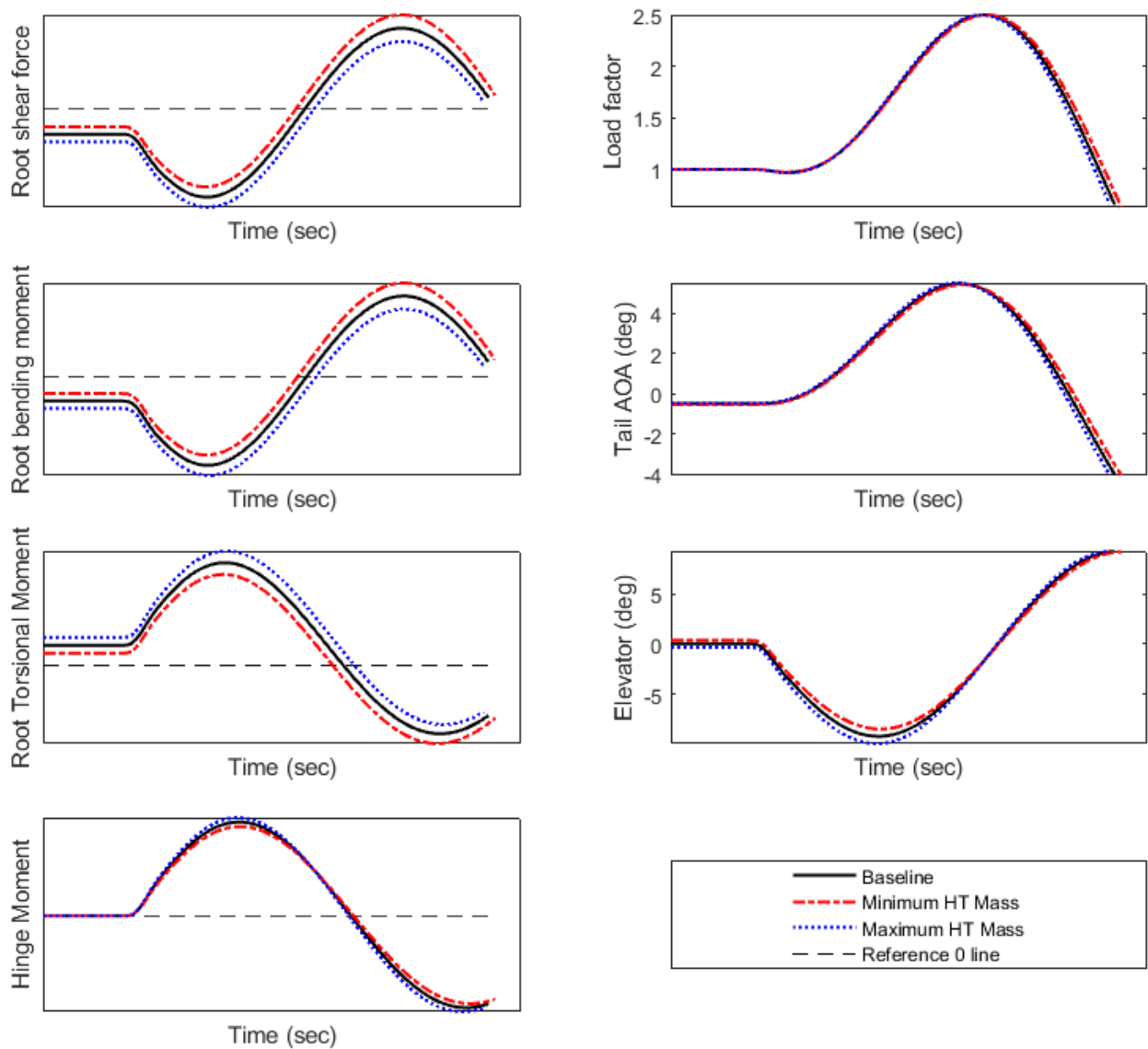


Figure 9: Time histories for sensitivity analysis of horizontal tail mass

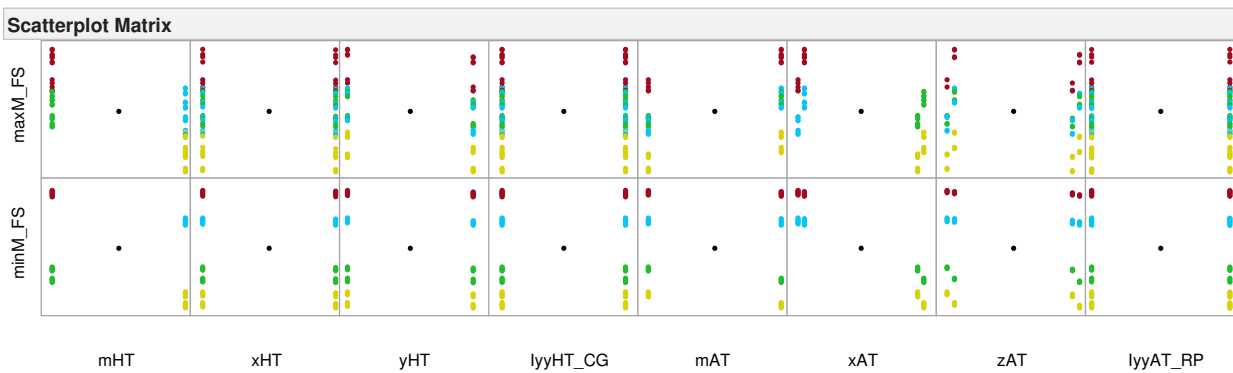


Figure 10: Scatter plot matrix of mass property screening cases showing bending moment

The factors that appear to have the most influence on the shear force and bending moments are $k_{C_{N\delta e}}$, $k_{C_{M\delta e}}$, $k_{C_{N\alpha}}$, $k_{C_{M\alpha T}}$. When $k_{C_{N\delta e}}$ and $k_{C_{M\alpha T}}$ increase, the maximum peak increases and the minimum

Table 5: Ranges of parameters varied during mass properties screening test

Coefficient	C_{N_0}	C_{N_α}	$C_{N_{\alpha T}}$	$C_{N_{\delta e}}$	C_{M_0}	C_{M_α}	$C_{M_{\alpha T}}$	$C_{M_{\delta e}}$	$C_{he,\alpha T}$	$C_{he,\delta e}$
Variation	$\pm 5\%$	$\pm 5\%$	$\pm 5\%$	$\pm 5\%$	$\pm 5\%$	$\pm 5\%$	$\pm 5\%$	$\pm 5\%$	$\pm 10\%$	$\pm 10\%$

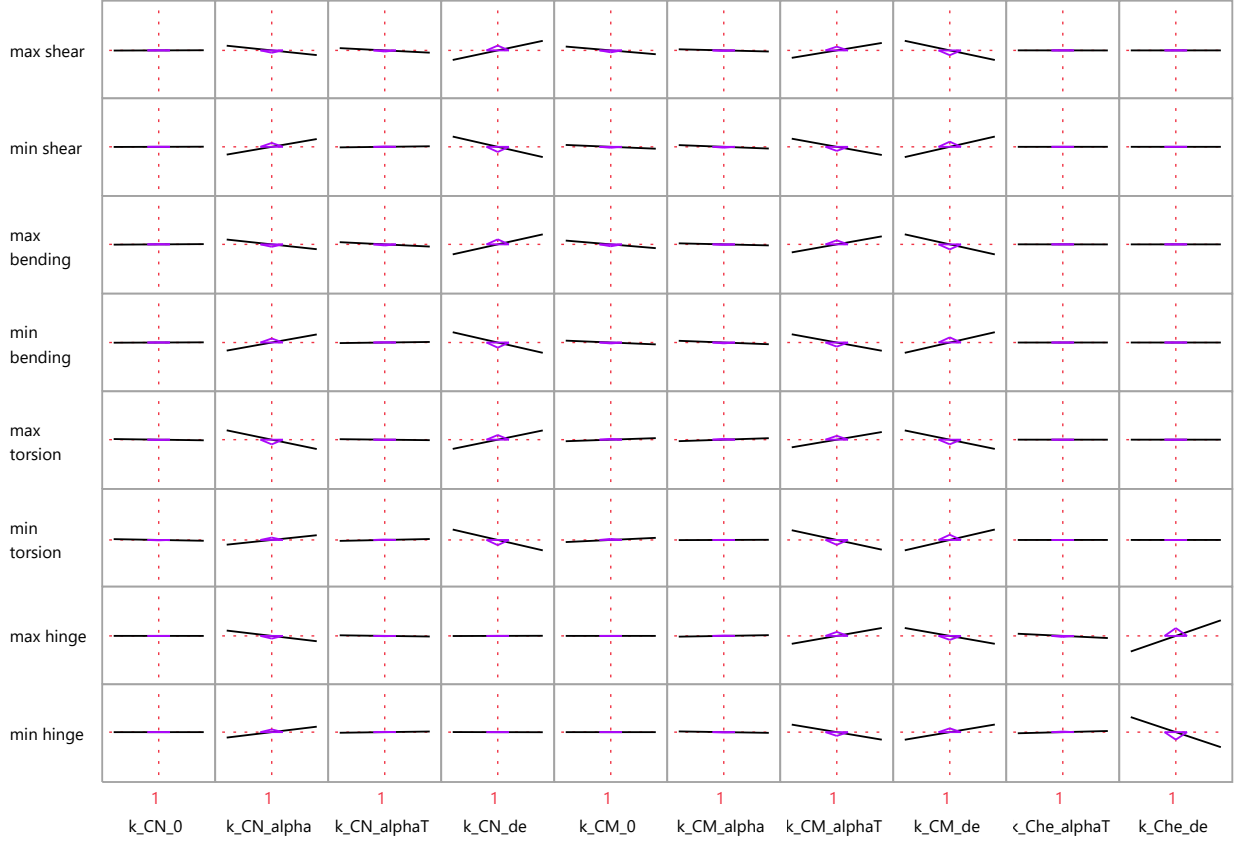


Figure 11: Profiler plot showing sensitivity to aerodynamic characteristics

peak decreases in value, leading to a net effect of increased magnitude of both peaks of the shear force, bending moment, and torsional moment. Similarly, increasing the K-factor $k_{C_{M_{\delta e}}}$ decreases the magnitude of the loads. To better visualize this, sensitivity studies were conducted by varying one K-factor at a time. The time histories in Fig. 12 show the isolated effect of $k_{C_{N_{\delta e}}}$. The curves show an increase in magnitude with an increase in the coefficient which is consistent with the profiler. Similar plots were created for the other coefficients to verify the trends observed in Fig. 11. The hinge moment peaks show sensitivity to the previously described coefficients, as well as to $k_{C_{he,\delta e}}$. The K-factor $k_{C_{M_0}}$ has a small but noticeable influence on the root forces and moments.

Similar to the mass properties study, these interpretations were supplemented by scatter plot matrices. Figure 13 depicts the plots for the bending moment screening cases for a point in the flight envelope. Trends stand out for both $k_{C_{N_{\delta e}}}$ and $k_{C_{M_{\delta e}}}$ where the most significant shift up in maximum peak and shift down in minimum peak (red color) is obtained only at higher $k_{C_{N_{\delta e}}}$ and at lower $k_{C_{M_{\delta e}}}$.

Plots were generated and inspected for all 25 points considered in the screening process and for all load of interests. Following this analysis, the K-factors $k_{C_{N_0}}$ and $k_{C_{he,\alpha T}}$ were set to their default values and were not attributed any uncertainty in the following studies.

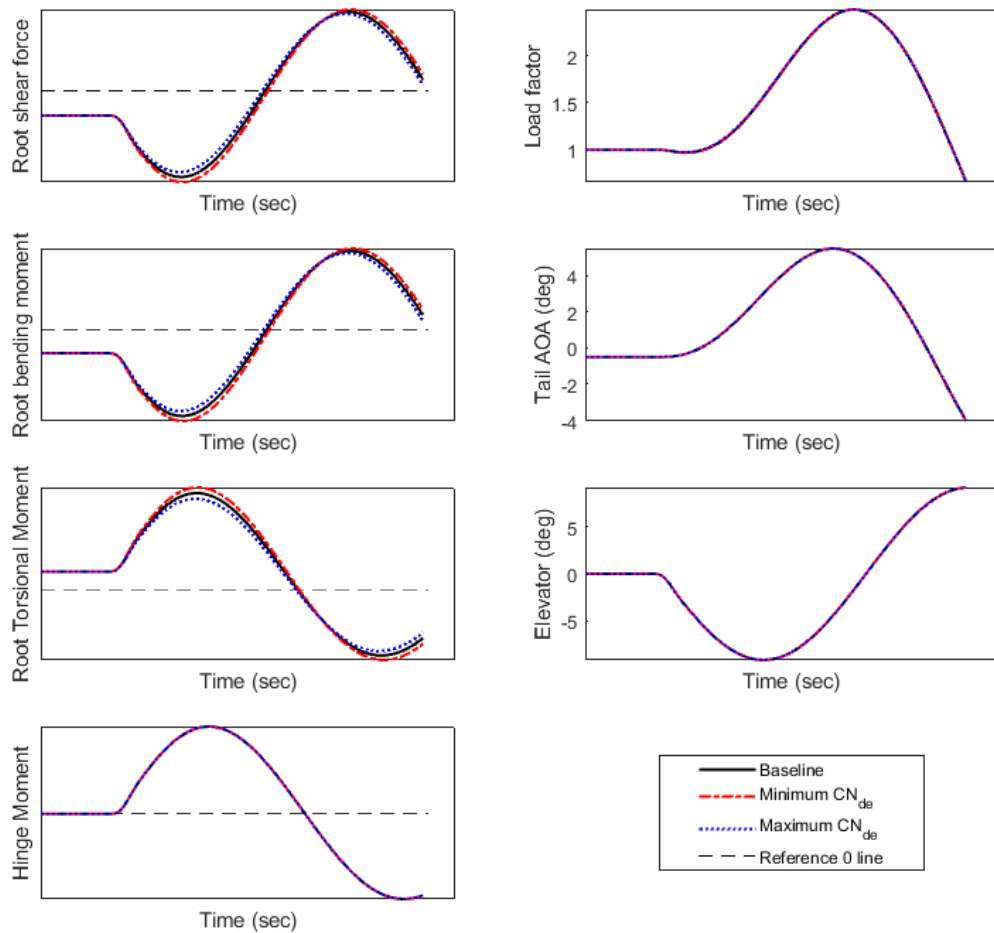


Figure 12: Time histories for sensitivity analysis of $k_{CN_{\delta e}}$

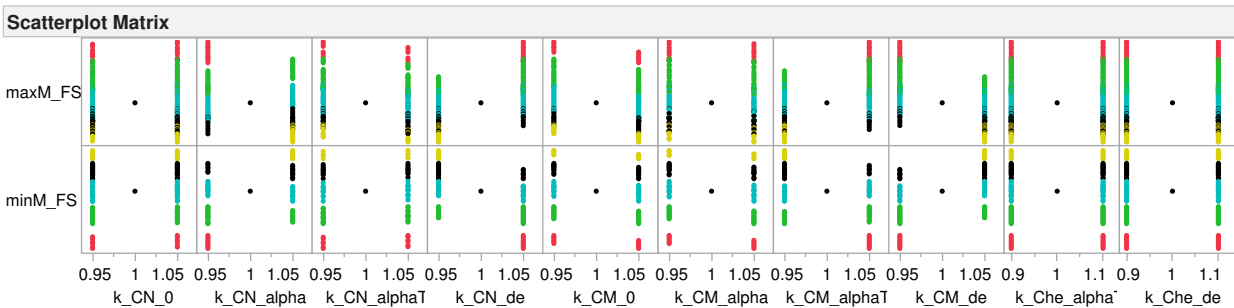


Figure 13: Scatter plot matrix of aerodynamic coefficients screening cases showing bending moment

V. Uncertainty Analysis

V.A. Method selection for uncertainty analysis

There are three main options for probabilistic analyses. The first one consists of performing a Monte Carlo analysis on the actual analysis code. The feasibility of this approach depends on the per-case run-time for the analysis code. The second option is performing a Monte Carlo study on a surrogate model that approximates the analysis code for the design space of interest. Naturally, this is significantly influenced by the accuracy of the developed surrogate model. The last one is to use the analysis code as is and approximate the Monte Carlo simulation itself through a Fast Probability Integration.¹⁰ Since the run-time of the simulation framework was not prohibitive, the first option was selected, obviating the need for and added complexity

of developing accurate surrogate models. A Monte Carlo simulation was then performed for all the points that resulted in the most critical loads across all weight conditions (Fig. 14).

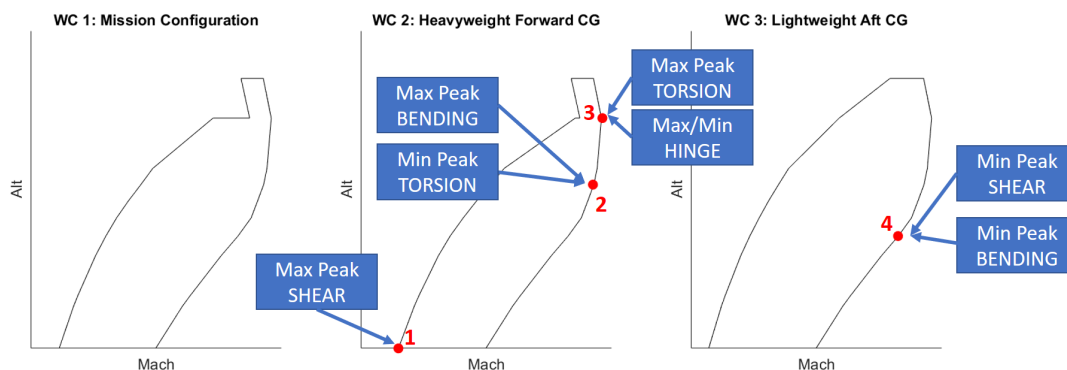


Figure 14: Points investigated in uncertainty analysis

V.B. Identification of probabilistic distribution of input variable

Several probability distributions were considered for each variable based on their advantages and limitations. The key characteristics considered were symmetry and shape. With input from subject matter experts, normal distributions were selected for all variables with the exception of the A-T mass. The mean for each of these normal distributions was the default deterministic value. While normal distributions extend to $\pm\infty$ with probabilities at the tails decaying asymptotically to zero, an additional constraint was put on the inputs in this study: minimum and maximum limitations. The ranges were imposed to extend only up to $\pm 3\sigma$ to ensure physical sense of the variations, while still retaining over 99.7% of the population in the distribution. Based on subject matter experts' input, a skewed distribution was employed for m^{A-T} . This ensured larger probabilities that the value sampled was higher than the mean. A beta distribution was selected, because of the ability to concurrently modify the range, dispersion (variability), and skewness.

For each of the four points in Fig. 14, a set of 10,000 cases was created by sampling random input parameters from their associated distributions. The deterministic analysis was then run for each of them, resulting in a distribution with a population of 10,000 data points for each of the results. The following results are presented in terms of percent changes of the responses from the reference (baseline) values.

Figure 15 shows the distribution of percent changes for all root loads and hinge moments for Point 1 as annotated in Fig. 14. The distributions for all four points can be found in Appendix A. This point corresponded to the maximum peak shear force in the deterministic analysis. From the histograms, this critical value varied by more than 30% when all the uncertainties were propagated. However, the standard deviation associated with this population was 8.28% which is indicative of the dispersion of this data around the mean of 0. Based on this population, over 99.97% of the cases will be within $\pm 24.84\%$ with higher probabilities towards 0%. As expected due to the Central Limit Theorem, these populations all resemble normal distributions. The data for all points is summarized in Table 6. The mean for all of them differed from zero by a negligible amount and was thus not tabulated.

Fig. 16 shows a scatter plot matrix of all the cases for Point 1. This figure illustrates trends regarding how the critical loads behave relative to one another. As expected, the shear force and the bending moment are highly correlated, as displayed by the cases lying on a line with ascending slope. While these plots focused on the peak values, it was important to understand how the variability affected the development of the loads throughout the maneuver. Fig. 17 shows the evolution of the four loads of interest for the default values. At 2.5 seconds time intervals, the vertical line shows the extent to which the loads varied at the given time step in all the 10,000 cases (for Point 1).

Additionally, each of these vertical lines can be better visualized as a box plot. This way, rather than looking just at the maximum range of variability - including outliers and values with very small percentages - one could see how far off from the baseline curve the data is concentrated. Fig. 18 illustrates a series of box plots for the shear force shown in the top right corner of Fig. 17. Each box plot corresponds to a vertical blue line from the previous plot. In this figure, the values shown on the vertical axis are the percent changes from

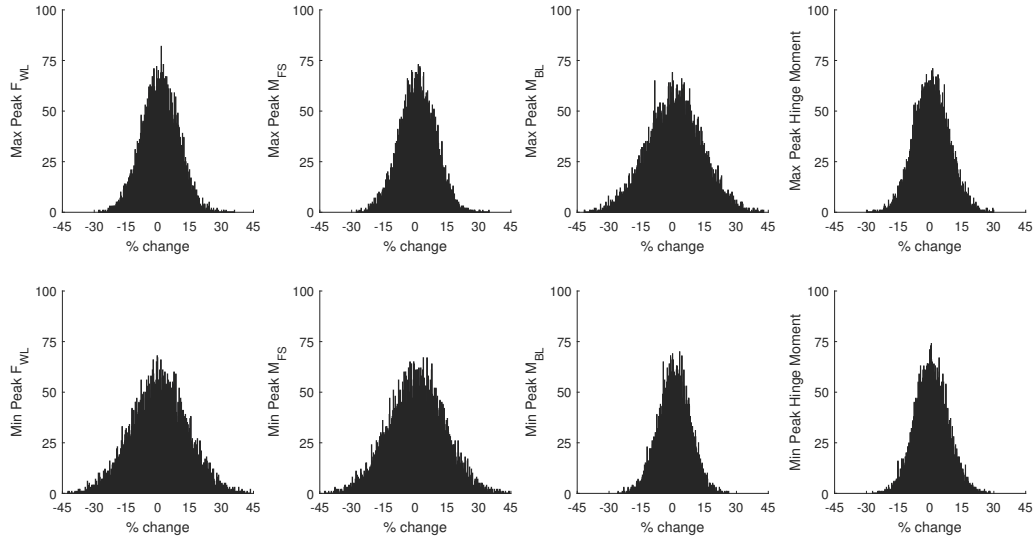


Figure 15: Histograms showing the percent change in each of the critical loads for Point 1

Table 6: Summary of Uncertainty Analysis Results for shear force (SF), bending moment (BM), torsional moment (TM) and hinge moment (HM)

	Point 1		Point 2		Point 3		Point 4		Critical
	Max %	σ (%)	Max %	σ (%)	Max %	σ (%)	Max %	σ (%)	
Max peak SF	36.11	8.28	42.89	11.39	42.18	10.07	39.89	10.67	1
Min peak SF	43.64	12.65	28.66	7.62	28.26	7.25	15.95	3.96	4
Max peak BM	34.72	8.16	38.38	9.98	39.19	9.76	50.27	13.28	2
Min peak BM	44.26	12.79	31.35	8.41	28.95	7.42	17.02	4.24	4
Max peak TM	42.88	12.38	46.54	12.08	31.24	7.88	29.41	7.30	3
Min peak TM	26.39	7.21	24.95	6.36	26.15	7.16	88.51	23.96	2
Max peak HM	29.83	7.97	21.21	5.49	21.29	5.44	22.60	5.11	3
Min peak HM	28.20	7.40	21.40	5.56	21.76	5.53	22.46	5.09	3

the baseline value at that time step. The blue box indicates where 50% of the data lies, with the bottom edge being the 25th percentile and the top edge the 75th percentile. The median aligns well with the 0 mark and at most time steps indicated, half of the data lies within 20% and even 10% of the baseline value.

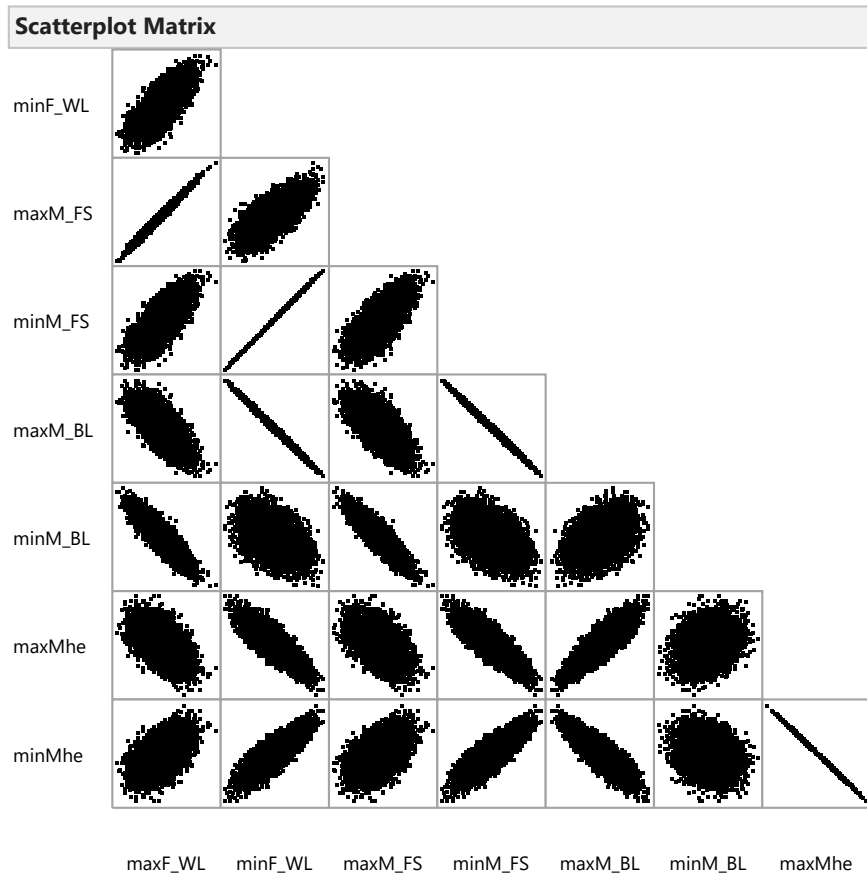


Figure 16: Scatter plot matrix showing correlations between loads

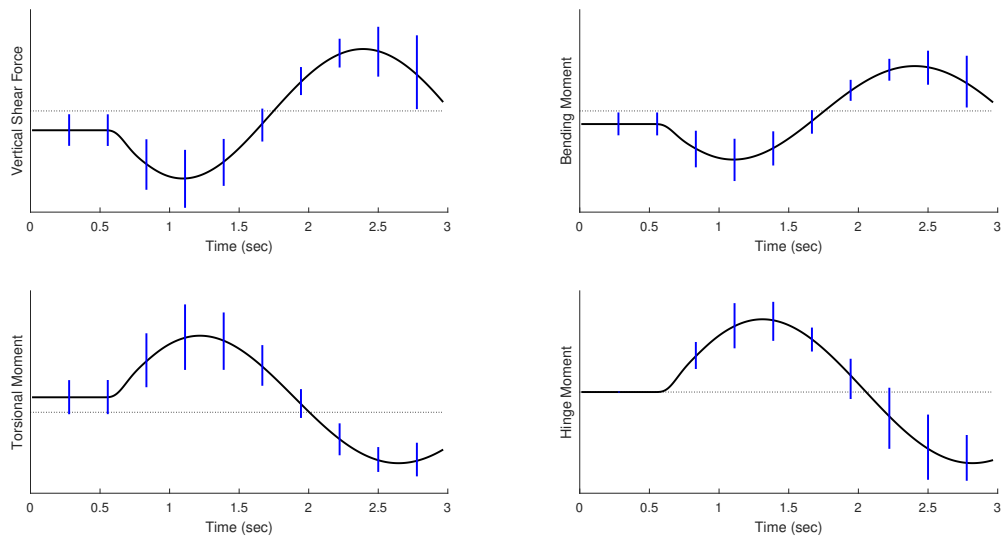


Figure 17: Time histories of loads with variation due to uncertainty shown at 2.5 seconds intervals

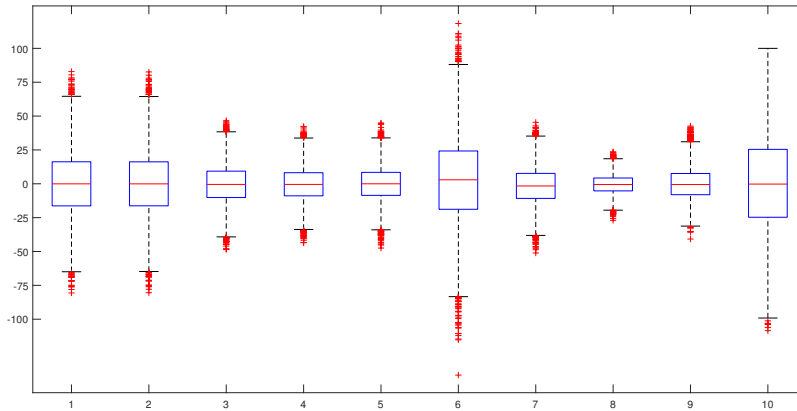


Figure 18: Box plots showing variation of shear force at a selected number of time steps

VI. Conclusion

In this work, a framework for simulating dynamic maneuvers specified by the Federal Aviation Regulations and obtaining the resulting structural loads on the empennage was enhanced to speed-up simulation time and allow for uncertainty analysis. A methodology was developed and demonstrated to propagate variation in values of mass and aerodynamic properties through the simulation. Screening and sensitivity analysis revealed that the mass properties that significantly affect the loads are the horizontal tail mass, the mass of the aircraft minus tail, and the x-coordinate of the aircraft minus tail, followed by smaller effects arising from tail CG coordinates in the x and y directions. Among aerodynamic properties, the factors that appear to have the most influence on the shear force and bending moments are the ones associated with elevator deflection derivatives as well as the normal force derivatives with respect to angle of attack and pitching moment coefficient with respect to angle of attack of the tail. When multiple factors were varied simultaneously, the variability was shown to grow significantly. It was seen that variation in critical root structural loads was more than 30%. Such insights are not readily apparent from a single-point deterministic analysis.

Acknowledgments

The authors would like to thank and acknowledge the following representatives from the Gulfstream Aerospace Corporation in Savannah, Georgia for their technical guidance and oversight during the course of this work: Mr. Robert Martin (Engineering Manager - Loads, Dynamics, & Mass Properties), Mr. Mark Ray (Staff Scientist - Loads & Dynamics), Mr. James Senter (Group Head - Loads & Dynamics), and Mr. Philip Riek (Engineer - Loads & Dynamics).

References

- ¹National Transportation Safety Board, N. T. S. B., “Aircraft Accident Report NTSB/AAR-04/04,” <https://www.ntsb.gov/investigations/AccidentReports/Reports/AAR0404.pdf>, [Online; accessed 29 October 2017].
- ²Federal Aviation Administration, U. D. o. T., “Code of Federal Regulations, Title 13, Part 25: Airworthiness Standards: Transport Category Airplanes,” <http://www.ecfr.gov>, [Online; accessed 26-October-2016].
- ³Mares, C. and Ursache, N., “Aircraft Ground Structural Testing,” *Encyclopedia of Aerospace Engineering*, Vol. 1-16, 2014.
- ⁴De Florio, F., *Airworthiness: an introduction to aircraft certification*, Elsevier, 2010.
- ⁵Gael, G., Duca, R., Sarojini, D., Shah, S., Chakraborty, I., Briceno, S., and Mavris, D. N., “A Simulation-Based Framework for Structural Loads Assessment during Dynamic Maneuvers,” *The AIAA Aviation and Aeronautics Forum and Exposition (AIAA AVIATION Forum) 2017*, 2017.
- ⁶Cruise, T. A., *Reliability-Based Mechanical Design*, MARCEL DEKKER, INC., 1997.
- ⁷Lambe, A. B. and Martins, J. R., “Extensions to the design structure matrix for the description of multidisciplinary design, analysis, and optimization processes,” *Structural and Multidisciplinary Optimization*, Vol. 46, No. 2, 2012, pp. 273–284.
- ⁸FlightGear, “A free flight simulator,” <http://www.flightgear.org/Docs/FGShortRef.html>, 2016, [Online; accessed

26-October-2016].

⁹Delaurentis, D. A., *A probabilistic approach to aircraft design emphasizing stability and control uncertainties*, Ph.D. thesis, Georgia Institute of Technology, 1998.

¹⁰Mavris, D. N., "A "Paradigm Shift" in Complex System Design: Enabling Technologies for Strategic Decision Making of Advanced Design Concepts," September 2016.

Appendix A - Distributions of percent changes for all loads and points

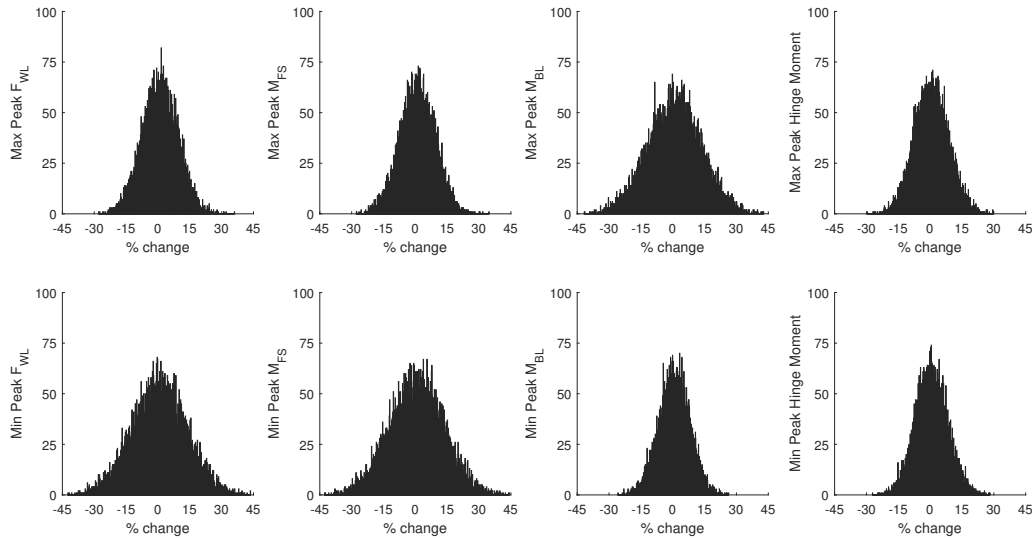


Figure 19: Histograms showing the percent change in each of the critical loads for Point 1

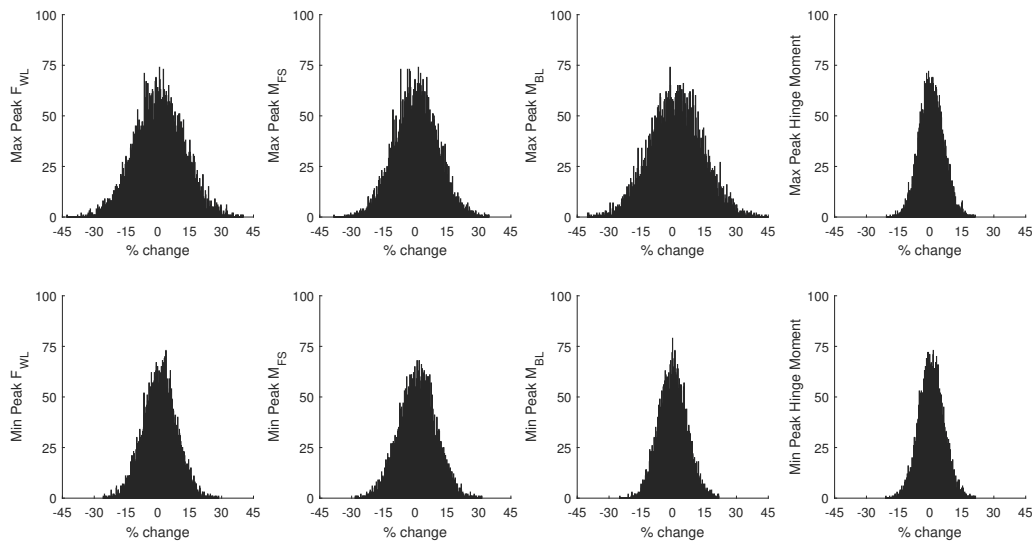


Figure 20: Histograms showing the percent change in each of the critical loads for Point 2

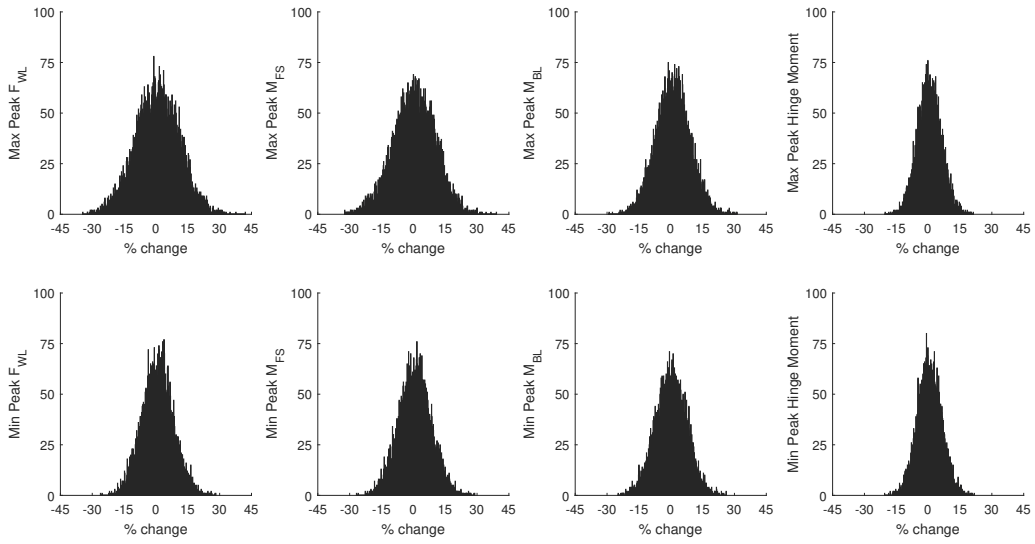


Figure 21: Histograms showing the percent change in each of the critical loads for Point 3

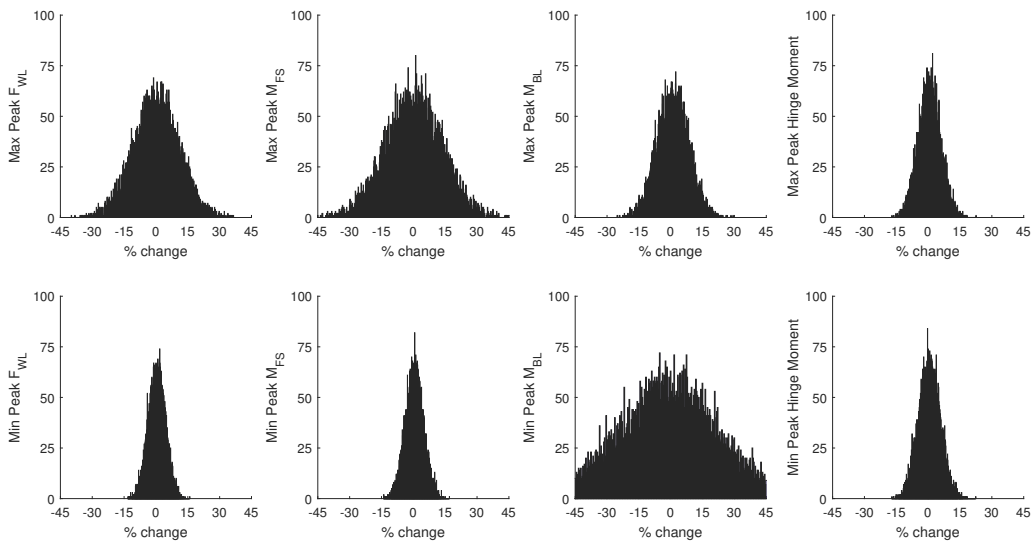


Figure 22: Histograms showing the percent change in each of the critical loads for Point 4